Flow Measurement and Instrumentation 111 (2026) 103454

Contents lists available at ScienceDirect

Flow Measurement and Instrumentation

journal homepage: www.elsevier.com/locate/flowmeasinst

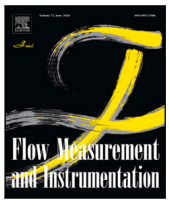

Numerical design and CFD validation of a low Reynolds number orifice flow meter

Victor Pozzobon

Université Paris-Saclay, CentraleSupélec, Laboratoire de Génie des Procédés et Matériaux, Centre Européen de Biotechnologie et de Bioéconomie (CEBB), 3 rue des Rouges Terres 51110 Pomacle, France

ARTICLE INFO

Keywords:
Flow meter
Low Reynolds number
CFD
Laminar
Transition

ABSTRACT

This work aims at designing an affordable digital flow meter suitable for air flows encountered in biotechnology laboratories (10 to 1,000 Nml/min, in 4 to 8 mm diameter pipes, under 1 to 8 bar). It builds on the classical orifice flow meter designs (pressure difference-based and robust) and recent pressure sensors improvement (allowing one sensor to measure from 1 to 10,000 Pa). While orifice flow meters are well-established for turbulent regimes, owing to their ability to deliver an almost constant discharge coefficient value, their application in low Reynolds number conditions (such as the ones above) is underrepresented. In these conditions, the pressure difference strongly depends on the Reynolds number, potentially posing a challenge. To address it, this article aims to derive design guidance for low Reynolds number cases, using a numerical workflow, based on the CFD framework OpenFOAM. Taking advantage of recent turbulence development of transitional turbulence, it is able to cover laminar, transition, and turbulent regimes. The predictions were extensively validated against experimental data (average MAPE of 5.43 %, NSE of 0.98, and CCC of 0.99). Once confidence has been built, the numerical workflow was used to explore the targeted design-space (β ratio from 0.0375 to 0.10, t^* ratio from 1.0 to 2.0, and Reynolds number from 1 to 400). Results aligned with established design principles: a low β ratio and high dimensionless thickness (t^*) are needed to ensure a measurable pressure difference. Two candidate designs emerge: $\beta = 0.11$ and $t^* = 1.75$, and $\beta = 0.0625$ and $t^* = 1/8$. Still, from a practical point of view, a machining tolerance analysis showed that realizing the optimal system could be quite a feat. Specifically, it requires drilling a very small orifice diameter (0.25 or 0.44 mm) while demanding tight machining tolerances ($\pm$ 0.01 mm), making fabrication non-trivial. Overall, the study demonstrates that a low Reynolds number orifice flow meter for biotechnology applications is technically feasible, but its practical implementation requires precise manufacturing or external calibration of each of the units.

1. Introduction

Numerous fields of engineering involve gas delivery to a system. In some cases, this gas supply has to be finely controlled, while in some other cases, an approximate value ($\pm$10%) is sufficient. Industrial bioprocesses fall into the second category for several reasons. First, the employed gas is air, most of the time. Hence, it is a readily available and low-cost commodity that has no chance of hindering the process's economic balance. Second, gas flow rate is not the primary lever of gas transfer modulation in bioprocesses. Indeed, usually, acting on the gas flow rate, even to a large extent, only induces a minor improvement in gas dissolution and can even be detrimental, *e.g.*, flooding the stirrer. On the contrary, agitation is the main operation variable, as it allows for efficiently modulating bubble dispersion. Third, supplying excess air is favorable in almost any biotechnological process. For example, in the case of classical aerobic respiration processes, it prevents the microorganisms from producing undesired byproducts (such as acetate by *E. coli* when lacking oxygen). Therefore, air is classically blown in excess in the early stages of the culture (when biomass content is low), then at full capacity in the late stage (when biomass content is high and the culture is intentionally restricted in carbon source to maintain a favorable carbon/oxygen ratio, avoiding byproducts) [1,2]. Another example of this need for excess air can be found in large-scale photosynthetic cultures. Indeed, efficient microlagae cultures can accumulate molecular oxygen (originating from photosynthesis) up to toxic levels (above 200 to 300% of the saturation). Therefore, sparging high air flow rates is a strategy to lower the culture oxygen content [3]. Finally, even the Crabtree-positive yeasts (*e.g.*, *Saccharomyces cerevisiae*) benefit from increased oxygen delivery over their fermentative stage, even though slightly [4].

E-mail address: victor.pozzobon@centralesupelec.fr.

https://doi.org/10.1016/j.flowmeasinst.2026.103454
Received 11 March 2026; Received in revised form 13 June 2026; Accepted 17 June 2026
Available online 22 June 2026

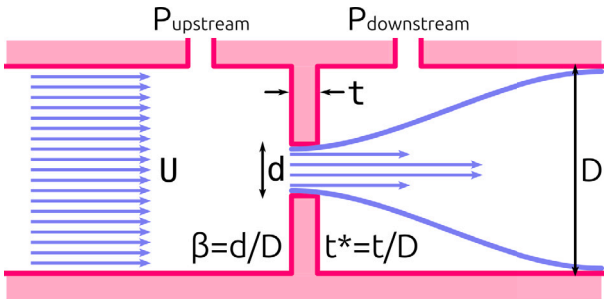

Fig. 1. Simplified schematic of an orifice flow meter with the essential characteristics. Scaling is intentionally inaccurate and was reduced for the sake of compactness.

In a nutshell, an exact regulation of the air flow rate is not strictly needed in a bioprocess context. An affordable sensor operating within an adequate range and allowing for data logging would be sufficient for process monitoring. Still, such sensors are challenging to find, especially in the range of interest for laboratory bioprocesses (10 to 1,000 Nml/min). Flow metering solutions classically encountered in biotechnology laboratories are: rotameters, which can be reasonably priced but do not allow for data logging, and mass flow controllers, which are expensive and may be too capable for the intended use. This work aims to explore alternatives with the hope of finding an intermediary solution. While, many other options, of varying complexity and accuracy, exist, and the kind reader is referred to Frank M. White's book (chapter 6) for an extensive review [5]. This work will focus on the orifice flow meter, as they possess advantages uniquely alleviating the constraints imposed by a biotechnology environment: convenient handling of moist gases, operation under high pressures, robustness against foam/culture backflows, ease to clean, to name a few.

An orifice flow meter is a monitoring system based on the pressure drop across a flow restriction. Classically, the restriction is a plate featuring a round hole placed in the center of a circular tube. This ease of conception allows such a flow meter to be affordable, relatively easy to manufacture, and robust (no moving parts). Therefore, it is not a surprise that they garnered a lot of attention and have been studied for almost a century now [6,7] and have been applied in a wide variety of contexts beyond flow monitoring. In details, what is making this technique popular in the industry is an highly convenient trait: the discharge coefficient (Cd) is almost constant in the turbulent flow regime, with a value of 0.6 [8]. Consequently, pressure drop and flow rate can be related in a reliable manner. This very favorable behavior also explains why most of the works on this type of flow meter have focused on the turbulent regime, up to a point where it has been standardized by the International Organization for Standardization (ISO) [9], for Reynolds numbers above 5,000 (based on the pipe diameter).

Comparatively, the laminar regime has received far less attention. Indeed, under such conditions, the discharge coefficient evolves with the Reynolds number as it is the result of the blending of two phenomena: the friction losses and the restriction losses. This somewhat unfavorable behavior was identified quite early in technology development by Johansen [6] and reviewed by Merritt almost four decades later [8]. It is of specific interest in the case at hand, as flow rates encountered in bioprocesses would fall into this category. Indeed, 10 to 1,000 Nml/min, in 4 to 8 mm internal diameter pipes, under 1 to 8 bar, leads to pipe Reynolds numbers ranging from 1 to 400.

Fortunately, this scientific landscape is not totally uncharted, and pioneering contributions are to be acknowledged. Among them, Johansen's one is paramount as it explained most of the system operating parameters, which can be summarized as follows. First of all, similarly to the turbulent regime, the system is governed by the β ratio, the t^* ratio, and the Reynolds number (Fig. 1). As a side point, the kind reader may note that, depending on the author and the physical considerations, the Reynolds number can be defined using the pipe diameter (when flow rate is considered) or the orifice diameter (when close the restriction hydrodynamic is considered). Independent of the β ratio, the discharge coefficient initially rises as 0.2 $\sqrt{Re}$ (orifice-based). Then, it overshoots with a magnitude depending on the β ratio, before stabilizing around 0.6 [6]. For round orifices, an orifice Reynolds number of 10 is considered the limit for the linear rise [8]. This point corresponds to when a laminar jet appears. It is followed by an unconditional transition to a turbulent jet regime for an orifice Reynolds number of 150 (even though the pipe Reynolds number is still low and the upstream flow is laminar). This succession of hydrodynamic events yields a complex behavior as acknowledged by Golijanek-Jędrzejczyk and Mrowiec in their experimental study [10] or by Borutzky et al. when the attempted different empirical modeling approaches [11]. Their goal was to assist scholars and engineers who may mistakenly choose a value of 0.6 for the discharge coefficient in low Reynolds number flow, leading to measurement errors. Still, modeling has not only been used in an empirical manner. Indeed, given the intricacy of the system, Computational Fluid Dynamics (CFD) has also been employed.

Similarly to the experimental investigations, CFD modeling of the system tends to focus on turbulent configurations, as they are of primary interest from an applicative point of view. Not only do the technique allows for reproducing experimental results and obtaining a detailed understanding of the flow pattern (*vena contracta*, reattachment length, ...), but it also allows for the design of new systems [12]. Finally, it can helping spotting some limits of the system that are difficult to access experimentally, such as the possibility of a compressibility effect (with Mach number reaching 0.3) at the orifice level [12,13].

Focusing on numerical studies dealing with the laminar regime, one can note the work of Sahin and Ceyhan [14], later expanded by Tunay et al. The first team has been able to reproduce the results of Johansen numerically, for an orifice Reynolds number below 150 (using an in-house finite difference code). Then, the authors studied the influence of the orifice thickness (from 1/16 to 1/2 pipe diameter) on the system behavior experimentally (discharge coefficient only) and numerically (flow pattern). They showed that a dimensionless thickness of 1/8, or more, leads to a reattachment of the flow within the orifice. Extending these investigations, Tunay et al. explored the system behavior in both laminar and turbulent regimes [15]. They have been able to identify that increasing the orifice thickness widens the jet diameter and, consequently, shortens the reattachment length. Also, the asymptotic behavior of the system is not altered, and the discharge coefficient converges around 0.6. While insightful, this study lacks critical details, such as the management of the laminar/turbulent flow cooccurrence or the required domain size (upstream to capture flow acceleration, and downstream for the fully developed outflow condition to be valid). Nevertheless, they showed that mainstream CFD codes were mature enough to tackle this problem.

While, until now, dimensionless quantities, agnostic to the fluid itself, have been discussed in this introduction, it is also important to consider the fluid nature in practical cases. Indeed, because of their density, liquids will naturally induce a higher pressure drop across the system, allowing for an easier operation compared to gas. Also, compressibility effects can be neglected in liquids, while they may matter in the case of gases. This observation leads to an interesting and favorable behavior described in Page et al. seminal work [7]. By inducing a downstream pressure at least 0.53 times lower than the upstream pressure (for air, as $\gamma = 1.4$), the flow rate through the orifice becomes independent of the downstream pressure. It conveniently limits the need for pressure monitoring to the upstream section. This trait, while elegantly reminding that the compressibility has to be kept in check, also underlines the challenges associated with the application of orifice flow metering to gaseous fluids: low pressure drop for low

flow rates and compressibility for high flow rates, even though this is quite far from the intended application here.

For the sake of completeness, multi-hole and slot orifice flow meters are also to be mentioned, as they are a slight modification of the technique. The rationales for these designs are broad, ranging from pressure drop management [16,17] and reduced sensitivity to upstream flow disturbance [18], to multiphase flows [19], which can exhibit very specific flow patterns (segregated flow upstream and mist downstream). Also to be mentioned are the exotic use cases of orifice flow meters, as they have been applied to non-Newtonian flow viscosity measurement [13], microflow rate measurement (0.1 to 200 μL/s, through 20 μm holes) [20], and rate of atmosphere change in food packaging (though pinhole) [21].

The objective of this work is to investigate numerically the possibility of designing an orifice flow meter adequate for bioprocess laboratory applications, as done for their own fields by other authors [12,13]. Still, this objective poses a challenge not tackled to date: modeling the system in a transition regime. With this aim in mind, the OpenFOAM open source CFD framework will be used as it allows for an easy and wide spread of the results. Simulations will be run in laminar, transition, and turbulent regimes and compared to experimental data to validate the CFD predictions and the relevance of the selected models. Finally, once confidence has been built, the tool will be used to modulate classical orifice flow meter design so that it serves the needs of a bioprocess laboratory.

2. Numerical methods

2.1. Governing equations

This work assumes that the system's (Fig. 1) behavior can be modeled as the incompressible flow of a Newtonian fluid. While the second assumption stands for air under practically any circumstances, the incompressibility assumptions will have to be checked a posteriori, by verifying that the Mach number stays below 0.3, especially at the orifice level. With this set of assumptions, the Navier–Stokes equations can be used to describe the system. In this case, the dimensionless variant of the continuity equation and the momentum equation is used:

$$\nabla^* \cdot \mathbf{u}^* = 0 \tag{1}$$

$$\frac{\partial \mathbf{u}^*}{\partial \tau^*} + \nabla^* \cdot (\mathbf{u}^* \otimes \mathbf{u}^*) = -\nabla^* p^* - \nabla^* \cdot \mathbf{S}^* \tag{2}$$

with the following scalings:

$$\mathbf{x}^* = \frac{\mathbf{x}}{D}, \quad \tau^* = \frac{\tau U}{D}, \quad \mathbf{u}^* = \frac{\mathbf{u}}{U}, \quad p^* = Eu = \frac{p}{\rho U^2}, \quad Re = \frac{\rho U D}{\mu} \tag{3}$$

This formulation is intentionally general as it will have to deal with the three flow regimes encountered in this work: laminar, transition, and turbulent. While laminar flow modeling is straightforward, details regarding transition and turbulent flow have to be described. Based on the literature review, laminar and turbulent flow (turbulent jet) coexist for an orifice Reynolds number of 150 and above. So, the k-ωSSTLM model, introduced by Langtry and Menter [22], was used whenever the orifice Reynolds number exceeded 150, while the pipe Reynolds number remained below 2300. This model was introduced a decade and a half ago to allow scholars and engineers to resolve transition flows in a wide variety of contexts. Its two main features are a turbulence indicator field (γ) and a transition Reynolds number ($Re_{\theta t}$, based on momentum thickness) that conditions the onset of turbulence. Therefore, it allows for solving concomitantly laminar and turbulent flows (based on k-ωSST, for their turbulent part).

For cases featuring a pipe Reynolds number of 2300 and above, a fully turbulent flow was assumed, and the k-ωSST model was used [23]. This model differs from the one classically used for orifice flow meter simulation. Indeed, most authors used the standard k-ϵ [12,15,16,24], without specific justification, or the RNG-k-ϵ model [18], even though the Reynolds number remained moderate, around 36 000, while the model was developed for high-shear configurations [25]. Still, a reason for this choice might be that the model performed well on the backward-facing step benchmark, which is relatively similar to the case at hand. Despite the introduced dissimilarity with the community, this work relies on the k-ωSST model to describe turbulence, as it allows for maintaining consistency with the model used to approach transition cases, while reinforcing the originality of this work by applying a different turbulence model.

2.2. Internal geometries & computational domain dimension

In this work, the pipe is considered circular. The orifice is placed along the center line of the pipe and is circular. Consequently, the system was reduced to a 2D-axisymmetric domain (Fig. 2, detailed in the coming section). The two quantities that then define the system are β and t^* ratios. The β ratio was varied between about 0.2 and 0.8 to mimic the experimental setups in the case of the validation runs against Johansen's dataset. In a similar manner, the t^* ratio was varied between 1/16 and 1/2 when results were compared to Sahin and Ceyhan's experimental ones. No bevel was designed on the back-facing side of the orifice, as none of these two investigators reported using one. Finally, pressure monitoring was adjusted following their reports, *i.e.*, on both sides of the orifice for Johansen, and at a classical "D D/2" couple for Sahin and Ceyhan.

Experimental evidences and numerical practices suggest that, apart setting the β and t^* ratios, the computational domain size should be considered carefully. Johansen [6] visually noticed upstream perturbations to span over 0.5 pipe diameter. Still, the importance of the upstream pipe length does not lie in the orifice-induced perturbation, but in the need for having a fully established and swirl-free flow reaching the system. Consequently, the ISO standard advises for up to 65 pipe diameters, for flows having crossed several incidents upstream of the flow meter [9], while also suggesting the use of flow straighteners to shorten this length. Still, from a practical point of view, five to tens of diameters are usually employed experimentally (5 for [26], 12 for [17], 20 for [7], 37 for [19], 46 and 10 for [6], 170 for [14]). Similarly, downstream sections are also quite long (advised at a minimum of 6 pipe diameters by the ISO standard, the employed values ranged from 4 to 30, with an extravagant report at 140). The aim of these long downstream pipes is to avoid any perturbation that could alter the system through back-propagation.

From a numerical standpoint, those values are to be minimized, as computing excessively long domains would lengthen the calculations and increase their RAM impact. Furthermore, unperturbed flow, especially a laminar one, is quite easy to generate numerically. Therefore, authors used rather short domains (2.5 upstream, 7.5 downstream pipe diameters in [12], 21 and 3 pipe diameters in [15], 0.5 and 37 pipe diameters in [16], 10 and 10 pipe diameters in [18]) most of the time without justification. This lack of justification is somewhat problematic as the outflow conditions assume a fully developed profile, without verifying it. The same problem may arise when an inlet boundary condition is somewhat unknown, or not specified as its fully-developed profile, such as it is often the case for turbulent quantities (especially, dissipation rate, for more detail, the kind reader is referred to Merci et al.'s interesting work [27]).

Therefore, a 20 upstream and 20 downstream pipe diameters, 2D-axisymmetric domain was investigated to identify an adequate length. The objective was two fold: allow some pipe length for the inlet conditions to establish (especially in transition and turbulent regimes), and ensure that a long enough domain was simulated to ensure the validity of the fully developed outflow condition.

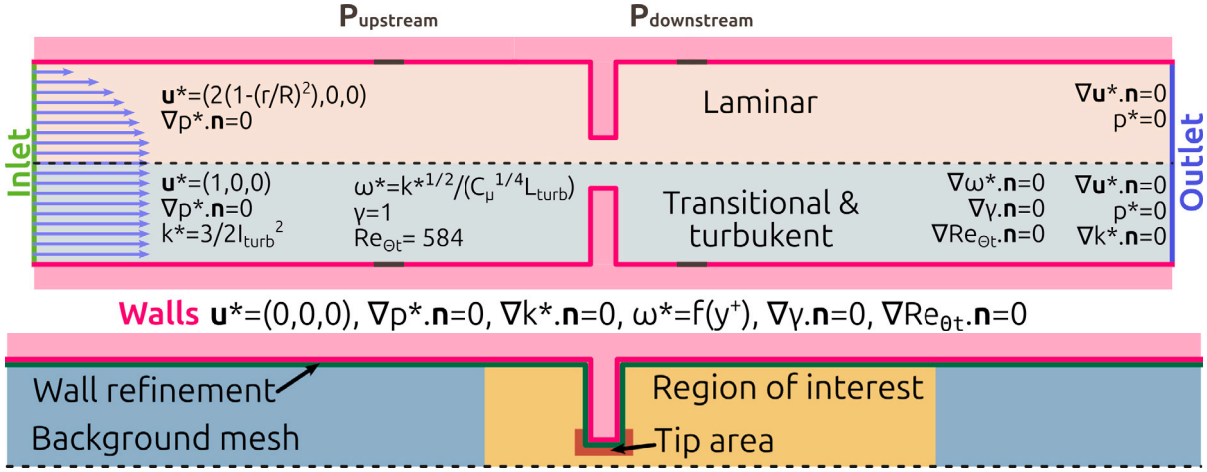

Fig. 2. Top - Simplified schematic of the geometry with the different boundary (color-marked) and the equations associated the different fields for laminar, transition, and turbulent cases. Bottom - Schematic of the computational domain with the areas marked for the specific meshing strategies. Scaling is intentionally inaccurate and was reduced for the sake of compactness.

2.3. Boundary conditions

The inlet of the pipe was described as a Poiseuille flow in laminar and transition regimes, while it was chosen as a flat profile in the fully turbulent regime, with a turbulence intensity of 7% [28] and a turbulent length scale of 7% of the pipe diameter [27]. In any case, the outlet conditions were chosen as those of a fully developed flow, which explains why extensive downstream length may have to be simulated to avoid introducing artifacts. A null velocity was imposed at the walls as well as the relevant wall functions for the turbulence-related quantity, *i.e.*, handling the viscous sub-layer when relevant (y^+-dependent). For transition cases, the value of the turbulence indicator field (γ) was set to 1 at the inlet, as advised by the authors of the model. The value of a momentum deficit Reynolds number ($Re_{\theta t}$) triggering the transition was set to 584, which corresponds to a turbulence intensity of 1%. This threshold was chosen based on the suggestion of the turbulence model authors' guidelines [22]. Yet, as the configurations tested here differ from the one considered for the model establishment, the value will be challenged and shown not to have any influence within a 0.1 to 10% turbulence intensity range (see Section 3.3). Finally, Fig. 2 (Top) displays the detailed equations as well as the boundary that applies to.

2.4. Numerical implementation

OpenFOAM v2506 was used to mesh the geometry and solve the set of equations. Depending on the cases at hand, *simpleFoam* (steady state) or *pisoFoam* (transient) solvers were used. Spatial and time discretization was led using second order schemes. In steady state, implicit and explicit under-relaxations were relied upon (coefficients between 0.7 and 0.95). Turbulence models and associated wall functions were drawn for the library. Turbulence model coefficients were checked to be in line with the referred publications. Regarding wall functions, previous research showed that their different variants yielded nondiscernible differences [24]. As this implementation of OpenFOAM relies on an implicit segregated approach to solve the system of equations, scaled residuals of 10^{-6} or below, for all fields, were considered sufficient to ensure convergence.

3. Validation

Before diving into the design of a new system, the robustness of the numerical tool must be validated. This stepwise process starts by ensuring mesh and domain independence, continues by ascertaining low sensitivity to the most uncertain parameters, and finishes with a validation against experimental data.

3.1. Mesh convergence

Mesh convergence was carried out under the most stringent conditions in an extended setup (20 diameters before and after the orifice). The conditions were set as follows in order to maximize the gradients, hence mesh requirements: pipe Reynolds number of 10^9, β of 0.2 (to maximize flow acceleration), turbulent intensity of 3.5% (0.5 × the reference value), and a turbulent length of 3.5% (0.5 × the reference value in pipe). The monitored outcome was the dimensionless pressure drop, *i.e.*, Euler number, between the two pressure taps.

The basic mesh setup was composed of 10 radial divisions per diameter, 10 axial divisions per diameter, with an expansion ratio of 2 in the radial direction (smaller cell close to the wall). This setup leads to a 2:1 ratio in the flow direction near the pipe axis. From this coarse setup, several variations were investigated to identify a mesh representing the best compromise between mesh size, accuracy, and computational time. This exploration was carried out in a systematic manner over different regions of the computational domain (Fig. 2 - Bottom). The first parameter to be tested was the initial mesh refinement (refined twice and thrice). Then, an increased local refinement in the region of interest (upstream compression - 2 pipe diameters before the orifice - and downstream wake - 6 pipe diameters after the orifice) was tested to better capture the flow acceleration and the wake (refined once to thrice). In addition, the effect of wall refinement was investigated (refined once to four times). Finally, mesh density in the vicinity of the orifice tip (box centered on the tip, spanning over 1/20 of the diameter in all directions) was also increased to finely capture the flow detachment (three to six refinement levels).

All in all, this systematic screening amounted to 217 simulations, the results of which are displayed in Fig. 3. For this setup, the theoretical value of the Euler number is 836.70. Indeed, assuming a pipe Reynolds number of 10^9 is a good approximation of the higher limit case, the value of Cd would reach $\pi/(\pi+2) = 0.6110$ [8]. The Euler number was preferred for this analysis as it magnifies the differences between configurations, while being easily linked to the discharge coefficient (Eq. (4)).

$$Cd = \sqrt{\frac{1-\beta^4}{2\beta^4 Eu}} \tag{4}$$

As one can see, most of the meshes reach a value of 750, or more, once a sufficiently large number of cells is used (above 25,000). Still, not all the strategies have the same effect, as underlined by the colored markers. Wall refinements (green markers) induce a high increase in the number of cells, while only moderately improving the predictions.

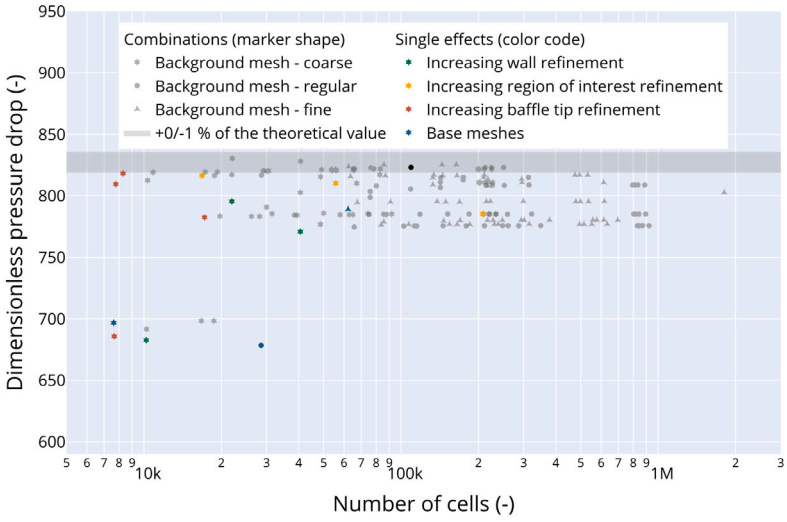

Fig. 3. Results of the mesh convergence analysis. Marker types - background mesh refinement. Colors - variations of a single parameter for the coarser background mesh. Shaded area - theoretical value +0/−1% area. β ratio of 0.2, t^* ratio of 1/12, domain size −20 to +20 pipe diameters.

Region of interest refinement (yellow markers) allows drawing nearer to the converged value at a lower cost, but it is tips refinement (red markers) that is the most effective. Still, when used individually, these strategies do not allow for predicting Euler numbers at least 1% close to the theoretical value. Furthermore, the kind reader will note that in some cases, extreme exploitation of a strategy leads to a diminution of the performance, *i.e.*, pushing a specific refinement procedure too far led to degraded predictions. While this may seem counterintuitive at first, it echoes CFD good practices, which advise not to impose an abrupt mesh resolution transition, at the risk of inducing mesh-related errors. Apart from practitioners' know-how, this behavior was demonstrated analytically, by Baker and van Meter, to originate from the difference in numerical precision in the advection scheme across the refinement interface [29] (even though guard cells are used, like in this work).

Overall, numerous meshes met the 1% deviation from the theoretical value criterion, rendering the ultimate choice quite open. The mesh with medium background refinement, followed by twice refinement steps in the region of interest and three at the wall and the tip level was retained (black dot). The rationale for this choice was that it smoothed the transitions between the different refinement zones of the mesh. Yet, many other possibilities could have been chosen and would surely have led to satisfactory results too.

3.2. Computational domain independence

Obtaining mesh-converged results is only the first part of the quality control of a CFD case. One also has to ensure that the domain is large enough to ensure that far-field conditions do not unduly influence the results. In the case at hand, two points are to be verified in terms of computational domain dimension. First, the velocity profile impinging on the orifice has to be established to match the experiments to be compared to. Second, the velocity profile at the outlet of the domain must also be established to agree with the chosen set of boundary conditions and avoid back-propagating any artifact. Therefore, the stability of the velocity profile was measured by comparing its evolution each one-diameter distance, over the domain. As velocity is a vector profile, the Root Mean Square Variation (RMSV) of the axial component was chosen as an indicator. One should note that this value is to be compared to the reference velocity to get a sense of its importance. As the simulations are performed in a dimensionless framework, the reference velocity is unity, easing the contextualization of the metric. Finally, as several configurations are to be simulated (β ratio from 0.2 to 0.8, laminar, transition, and turbulent flows), the domain independence has to be assessed for all of them.

Fig. 4 presents the RMSV for all the representative conditions. The first criterion (fully established profile impinging on the orifice) can be evaluated over the −20D to −1D domain. As one can see, the laminar flows fully develop in less than three diameters. The transition and turbulent conditions show no difference with respect to the β value in this section of the pipe, which is expected. In addition, they both require 10 pipe diameters to show a relative variation of less than 10^{-3} (with respect to a value of 1). Therefore, the inlet section of the domain can be considered long enough to avoid artifacts.

The second criterion (fully established profile at the outlet of the domain) can be evaluated over the +1D to +20D domain. Similarly to the inlet section, the laminar flows fully developed relatively rapidly once the orifice is past (in less than seven diameters). The transition and turbulent conditions show convergent trends with dependency on both pipe Reynolds number and β values. Still, once 20 pipe diameters are reached, the four profiles fell below the 10^{-3} threshold, ensuring the validity of the chosen set of outflow boundary conditions.

3.3. Sensitivity analysis

In order to ensure the robustness of the results, a sensitivity analysis was carried out. Inlet turbulent intensity (I_{turb}) and turbulent length (L_{turb}) were modulated by ± 50% in the case identified as the most sensible one during numerical prototyping, *i.e.*, a pipe Reynolds number of 5,000.

In addition, with the aim of testing the transition model, a case with a pipe Reynold number of 200 was chosen (laminar flow in the pipe and turbulent jet after the orifice). For this case, the value of the momentum deficit Reynolds number ($Re_{\theta t}$) triggering the transition was varied between 1,136 and 73, corresponding to turbulence intensities of 0.1 and 10%, respectively. The results of the sensitivity analysis can be found in Table 1. As one can see, despite a sizable variation in the inlet turbulence parameters, only a minor effect on the Euler number can be observed. These results can be explained by the fact that the k-ωSST has been designed to increase robustness with respect to freestream turbulence values, combined with the extensive pipe length, which allows ample distance for the flow to settle. These results align with those of Shah et al. who varied inlet turbulence intensity from 3 to 7% (reference value of 5%) and did not report any substantial variation in the simulation outcome (from −0.22 to +0.35% on the discharge coefficient value) [12]. Regarding the sensitivity towards the

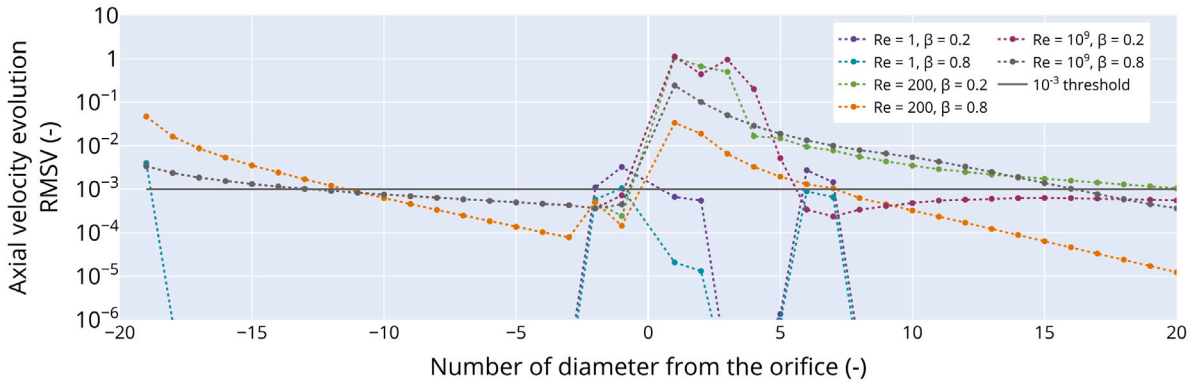

Fig. 4. Variation of the velocity profile over one diameter distances across the domain for β ratio if 0.2 and 0.8, laminar (Re = 1), transition (Re = 200), and turbulent (10^9) flows. Reynolds numbers are to be understood as pipe Reynolds numbers. The value at the orifice level is not calculated as the velocity vector profile does not span over the same diameter as the other profiles. t^* ratio of 1/12, domain size −20 to +20 pipe diameters.

Table 1
Results of the sensitivity analysis. Upper section - Sensitivity over the turbulence inlet value. Lower section - Sensitivity over momentum deficit Reynolds number triggering the transition. Case setup: t^* ratio of 1/12, domain size −20 to +20 pipe diameters.

Test case	Parameter span	Beta	Euler number				Variation coefficient
			Average	Standard deviation	Min.	Max.	
Re = 5,000	I = 3.5 to 10.5%	0.2	809.28	0.15	809.11	809.51	0.018%
	L_{turb} = 3.5 to 10.5%	0.8	1.3102	0.0117	1.2963	1.3285	0.893%
Re = 200	Transition turbulence intensity	0.2	672.86	0.30	672.60	673.18	0.044%
	I = 0.1 to 10%	0.8	0.78	0.00	0.78	0.78	0%

momentum deficit Reynolds number triggering the transition, it can also be deemed negligible. In the case of the β ratio of 0.2, this can be explained by the design itself, which forces flow acceleration and induces extreme shear at a very defined position, as opposed to a flat plate or a wing profile. In the case of the β ratio of 0.8, this can be explained by the fact that the acceleration is not sufficient to trigger a transition to turbulence. Therefore, the case features a laminar flow, showing, as expected, no sensitivity to the tested parameter.

3.4. Comparison with experiments - Johansen's dataset Cd=f(β)

Johansen's seminal dataset, published in 1930, was used to validate the numerical workflow predictions [6]. This dataset spans over orifice Reynolds number ranging from 1 to about 30,000 for β ratios of 0.209, 0.401, 0.595, and 0.794, and a t^* ratio value of 1/12. The experiments were carried out with different fluids, to ensure measurable pressure drops at low Reynolds numbers. As the data were available in a tabulated format, they were extracted manually using a dedicated software. Unfortunately, Johansen did report experimental uncertainty in his article. Therefore, an experimental accuracy of ± 0.025 on the discharge coefficient was assumed, as it is the one reported for modern days sensors at a pipe Reynolds of 10,000 [10,18].

Fig. 5 (Top) presents the comparison between experimental data (lines and shadings) and simulations (markers). The layout was chosen to match Johansen's one, *i.e.*, discharge coefficient versus the square root of the orifice Reynolds number. Contrary to the common practice, lines and shadings were used to draw experiments as it was found to enhanced readibility is this particular case. Finally, given the span of the dataset, the inset proposes a magnification of the low Reynolds configuration, where most of the discharge coefficient variation happens. As one can see, the agreement between the numerical predictions and the experimental data is good over the wide range of tested Reynolds numbers and β ratios.

Still, while confronting experimental and numerical discharge coefficient is a first step toward building strong confidence in the numerical workflow predictions, Johansen's work allows to go further. Indeed, the author also reported the physical characteristics of the flow. The main feature is the appearance of a *vena contracta* at sufficiently high Reynolds numbers. Johansen attributed it a contraction ratio of about 0.8, with respect to the orifice diameter, at a position of 0.1 pipe diameter downstream. The numerical workflow was able to reproduce the *vena contracta* (Fig. 5 (Bottom left)). Furthermore, in addition to reproducing, it predicted with an excellent agreement to Johansen's data: a contraction ratio of 0.81 (at the same position as Johansen) (Fig. 5 (Bottom right)). To demonstrate the robustness, another simulation (Reynolds of 20,000, and β ratio of 0.5) yielded a contraction ratio of 0.82. This consistency is a token of the robustness of the workflow.

Finally, Johansen also reported temporal characteristics of the flow. Indeed, he described that, in the case of a turbulent jet, large periodic structures could be observed at a regular interval of 1 pipe diameter downstream. These structures are likely to be the largest vortices originating from the jet external shear layer. This observation is in agreement with some theoretical work showing unconditional instabilities appear in the setup [30], but are not to be mistaken with acoustic effects that the system can induce [26]. Still, this type of structures cannot be reproduced by conventional RANS models. Therefore, an LES approach was deployed in an effort to validate the workflow capabilities as much as possible. The kind reader may note that the relevance of LES modeling in a 2D axisymmetrical setup will not be discussed here. From a technical standpoint, the Smagorinsky model ($Cs = 0.094$) coupled with van Driest wall damping was used to approach the phenomenon. The simulations were initialized with their RANS counterparts and were run for a time long enough to obtain a periodic behavior. Fig. 6 (Top) presents a visualization of a flow in the vicinity of the orifice for a β ratio of 0.5 (the same as Johansen for these observations) and a square root of the orifice Reynolds number of 150. The color map represents the dimensionless velocity fluctuations magnitude, while the isolines allow for vortices identification using the Q criterion [31]. As one can see, the vortices appear in the shear layer at the periphery of the jet. The structures become of a distinctive enough size about 1 pipe diameter downstream, which is Johansen's observation location. Moving from a qualitative appreciation of the

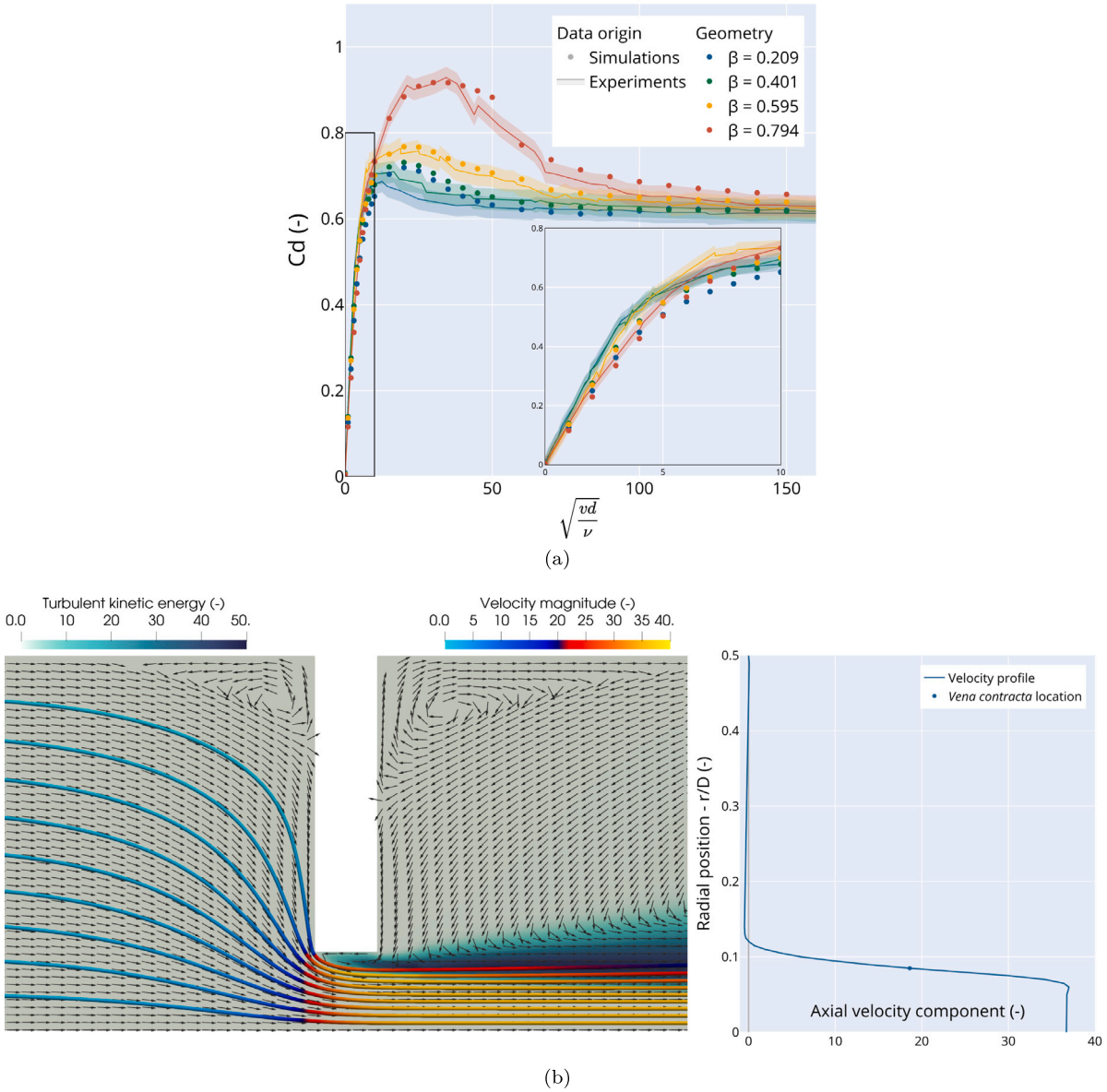

Fig. 5. Top - Experimental data (lines and shadings) extracted from Johansen's dataset and simulations (markers) carried out in this work. t^* ratio of 1/12, domain size −20 to +20 pipe diameters. Bottom left - Close-up view of the flow around the orifice for a β value of 0.209 and a square root of the orifice Reynolds number of 150. Color map - dimensionless turbulent kinetic energy. Vector field - velocity direction. Tubes - streamlines, colored by velocity magnitude. Bottom right - Axial velocity profile, 0.1 pipe diameter downstream. *Vena contracta* point extracted as the location of the mean between the extrema.

results, Johansen defined the Strouhal number of the phenomenon as $St = \frac{fd}{v}$, and obtained a stable value of 0.59 ± 0.04. By monitoring the pressure signal at the same location, and processing it using a Fast Fourier Transform, it is possible to recover the characteristic frequency obtained numerically (defined as the center of the top 90+ % intensity frequency band) (Fig. 6 (Bottom Right)). With this procedure, a Strouhal number of 0.52 ± 0.07 is obtained, which is in good agreement with Johansen's report. This is all the more true as the flow tends to expand in this zone, leaving the estimation of the frequency quite dependent on the probing location.

Finally, the quality of the LES simulation was assessed by computing the ratio of the resolved kinetic turbulent energy to the total kinetic turbulent energy (sub-grid kinetic turbulent energy computed as $(\nu_{sgs}/l_{sgs})^2$, with $l_{sgs} = C_s\Delta$). The results are presented in Fig. 6 (Bottom Left), where it can be seen that most of the domain is very well resolved (above 80%), while 3% of the volume is dramatically under-resolved, *i.e.*, where the vortices start to appear, in the vicinity of the orifice. Still, the mesh can be deemed adequate for the intended purpose.

3.5. Comparison with experiments - Sahin and Ceyhan's dataset Cd=f(t*)

Another dataset of reference worth comparing with is the one by Sahin and Ceyhan, who explored the effect of the t^* ratio for a β ratio of 0.5, while Johansen used a single t^* value and varied the β ratio. The two datasets are thus complementary. A major difference is that Sahin and Ceyhan restricted their investigations to the laminar regime (orifice Reynolds number below 150). Another difference is the definition of the t^* ratio the authors used, based on the orifice diameter, which is uncommon, and was converted to the classical $t^* = t/D$ definition in the present work. In a process similar to the one applied to Johansen's data, Sahin and Ceyhan's data were extracted manually. Fig. 7 presents their data and their numerical counterparts obtained with the proposed workflow. The presentation is the same as the one

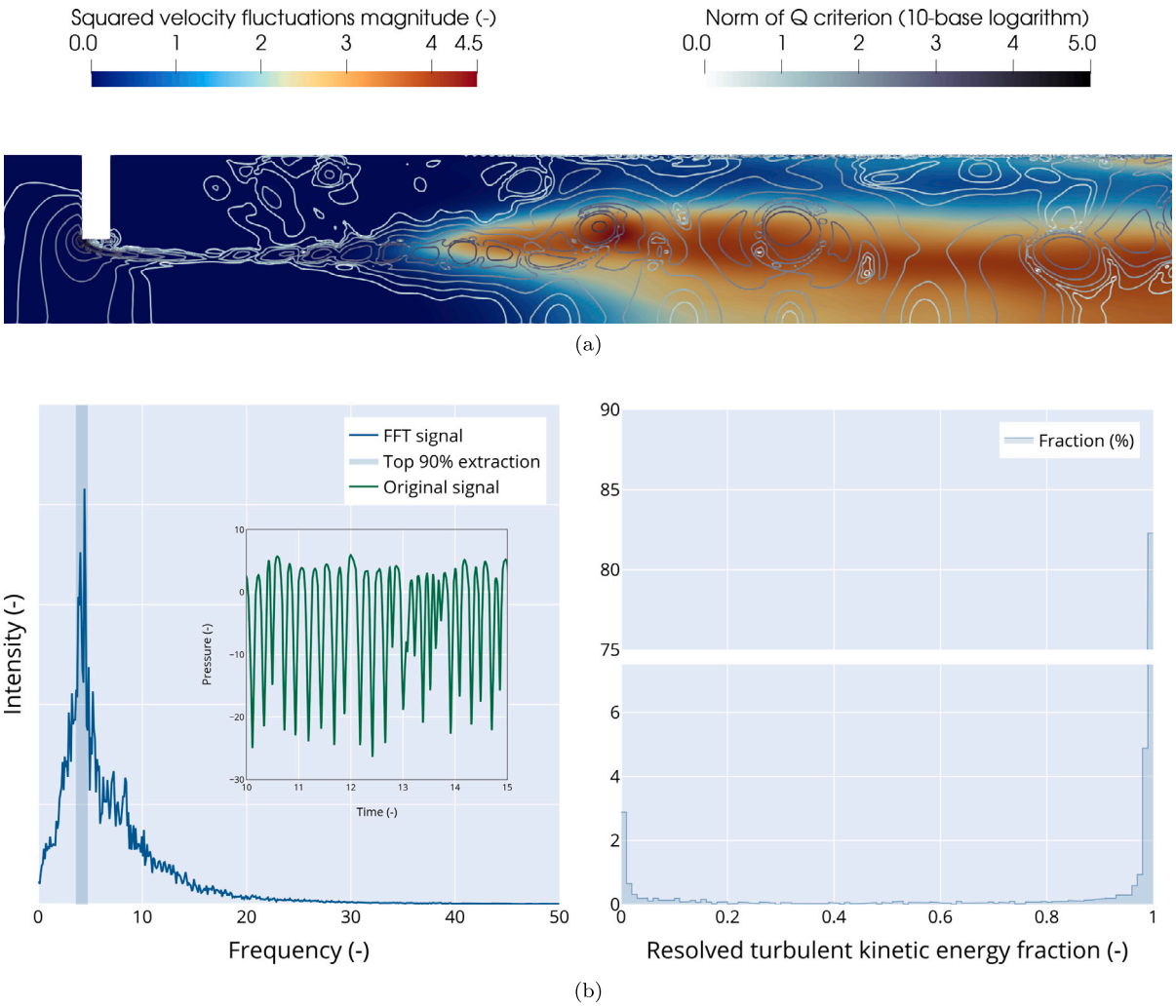

Fig. 6. Top - Close-up view of the flow around the orifice for a β value of 0.5 and t^* ratio of 1/12 and a square root of the orifice Reynolds number of 150. Color map - dimensionless velocity fluctuations magnitude. Contour lines - vortices location identified as Q criterion isolevels. Bottom Left - Pressure signal 1 pipe diameter downstream (5 dimensionless time units) at mid-height and its Fast Fourier Transform. Bottom Right - Resolved turbulent kinetic energy in the domain spanning from 0 to 1 pipe diameter downstream, 100 dimensionless time units after entering periodic regime.

chosen by the authors, *i.e.*, discharge coefficient versus the square root of the orifice Reynolds number. As one can see, the agreement between experimental measurements and numerical prediction is quite good.

In addition to their experimental exploration of the problem, Sahin and Ceyhan opted for a numerical approach to resolve the flow near the orifice. Their main conclusion is that as the t^* value increases, the magnitude of the *vena contracta* decreases up to a point where the detachment does not occur anymore. They identify this transition as happening when the t^* ratio increases from 1/16 to 1/8. Consequently, these configurations have been reproduced for the highest Reynolds number (most susceptible to detachment) with the presented workflow. Fig. 8 presents the flow field for three configurations: t^* = 1/16, t^* = 1/8, and t^* = 1/2. Paying close attention to the upper streamline inflection of the outlet of the orifice, one can see the flow stays attached to the inner part of the orifice from t^* = 1/8 and on, agreeing with Sahin and Ceyhan's calculations. Also, increasing the value of the t^* ratio leads to a more pronounced development of the velocity profile within the orifice (axial dimensionless velocity around 5.6 for t^* = 1/16, and 6.2 for t^* = 1/2), reinforcing the confidence one can have in the workflow.

3.6. Summary & assumption discussion

In addition to the aforementioned qualitative agreements, quantitative agreement, and summary of the span validation tests are presented in Table 2. Three metrics have been used to evaluate the ability of the workflow to reproduce the experimental data. The Mean Absolute Percentage Error (MAPE) measures absolute distance and yields a deviation percentage that is easy to interpret. The Nash–Sutcliffe Efficiency (NSE) allows for weighting for outliers owing to its quadratic nature and also offers an easy interpretation: close to 1 is good, 0 means using the average value of the observation would have delivered the same prediction, and a negative value is worse than using the average value [32]. The Concordance Correlation Coefficient (CCC) is an advanced metric that quantifies how similar two methods are (e.g., two analyzers processing the same samples, or, in this case, experimental readings and numerical predictions) [33]. A value close to 1 indicates good agreement, values close to 0 or negative values indicate poor concordance due to either systematic bias, reduced correlation, or both.

Still, while the agreement is good within the validation space, the coming sections will explore uncharted territory (in terms of β and t^* ratios), which requires further caution. First of all, regarding the mesh convergence, while it was validated for a β ratio of 0.2 and t^* ratio of

Table 2
Summary of the validation performance metrics over the two datasets and their respective operating conditions. MAPE - Mean Absolute Percentage Error. NSE - Nash–Sutcliffe Efficiency. CCC - Concordance Correlation Coefficient.

Dataset	β	t^*	Reynolds (orifice)	MAPE (%)	NSE	CCC
Johansen	0.209	1/12	1 to 30 000	10.2	0.95	0.977
	0.401			6.02	0.961	0.982
	0.595			3.54	0.976	0.988
	0.795			5.37	0.976	0.989
Sahin and Ceyhan	0.5	1/2	1 to 150	4.28	0.986	0.993
		1/4		4.13	0.988	0.994
		1/8		5.98	0.977	0.989
		1/16		3.90	0.988	0.994
Overall	–	–	–	5.43	0.975	0.988

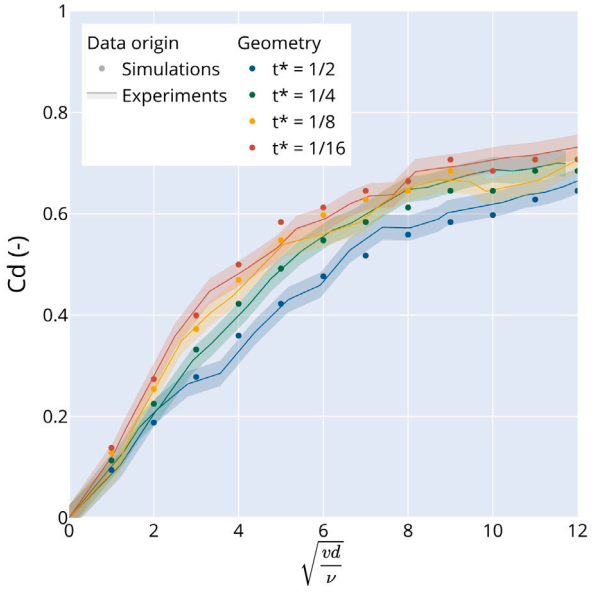

Fig. 7. Experimental data (lines and shadings) extracted from Sahin and Ceyhan's dataset and simulations (markers) carried our in this work. β ratio of 0.5, domain size −20 to +20 pipe diameters.

1/12, with a pipe Reynolds number of 10^9, it may not apply to the most extreme design cases: $\beta = 0.0375$ and $t^* = 1/8$, and $\beta = 0.08$ and $t^* = 2$. Therefore, an autoconvergence study on these cases was carried out using Celik et al. guidelines [34]. For the two cases, the extrapolated error was 3.23% and 0.34%, respectively. This level of convergence was deemed good enough to be confident in the results.

In addition to the adequacy of the meshing procedure, the incompressibility assumption is also to be challenged. To do so, the case featuring the smallest restriction and the highest volumetric flow rate (β ratio of 0.0675, flow rate of 1,000 NmL/min under 1 bar, in a 4-mm diameter pipe) was analyzed. In this case, assuming air to be at room temperature (20 °C – 293.15 K), the Mach number value reaches 5.7 10^{-2}. In addition, going further and accounting for the presence of a *vena contracta* with a 0.8 contraction ratio, the effective cross section gets further reduced, and the maximum Mach number value rises to 9.0 10^{-2}. Consequently, considerations about the fluid compressibility can safely be kept at bay.

Still, while the above assumptions could be validated, some are inherently tied to the chosen modeling approach, and their limitations are to be plainly acknowledged. For example, the turbulence models assume steady state turbulence, even in the transition regime, where intermittency can be encountered. Also, resorting to a 2D geometry can be criticized as turbulence in an intrinsically 3D phenomenon. Finally, while sensitivity to the most difficult to characterize boundary conditions has been analyzed, the effect of their potential variation in time was not assessed. Nevertheless, given the performance delivered by the workflow on the validation datasets, these limitations can be thought to be of marginal influence on the results at hand.

4. Application to system design

With enough confidence build thanks to the extensive validation of the workflow against other scholars' work, it is now time to apply the tool to design a measurement system for the intended application. The goal is to measure a flow of air, ranging from 10 to 1,000 Nml/min, in 4 to 8 mm internal diameter pipes, under 1 to 8 bar. These configurations lead to pipe Reynolds numbers varying between 1 to 400 (as the air dynamic viscosity does not depend much upon the pressure in the envisioned pressure range [35]). Therefore, laminar and transition regimes can be expected.

Now that physics and numerics have been considered, it is important to lay out clearly the design expectations. First and foremost, a satisfactory design will have to allow for at least 1 Pa pressure difference for the lowest flow rate. In terms of a dimensionless quantity, this requirement translates into a minimum Euler number of 6 10^5 (assuming air at room temperature, in the worst-case scenario, *i.e.*, minimum flow rate, maximal pressure, and pipe diameter). Second, the design has to be realizable, *i.e.*, to be at least plastic machining compatible. The rule of thumb taken here is that the hole cannot be less than 1/20 of the material thickness (*i.e.*, $t^* \leq 20\beta$), with a minimum diameter around 0.5 mm. Thirdly, as much as possible, the pressure vs. Reynolds number characteristic curve should exhibit a monotonic, relatively simple shape (linear, quadratic, ...), in linear or log–log scale.

Finally comes a preliminary delineation of the design space with envisioned designs and their confrontation with already established knowledge. The objective of this last point is to avoid simulating designs that can be ruled out a priori. The goal is to limit computational impact, provide easy-to-interpret results, and keep the article under a reasonable word count.

4.1. Potential designs

From the literature, four levers of action on the discharge coefficient can be identified: the β ratio, the t^* ratio, the number of holes, and the shape of the holes. Therefore, four designs can be envisioned (Fig. 9): the canonical one with a small β ratio, the high t^* ratio one, a multi-hole variation of the canonical design, a slotted orifice variation (not pictured), or a diverging one aiming at exacerbating the β ratio.

The first thing to be remembered is that resorting to multi-hole and/or slotted orifices tends to increase the value of the discharge coefficient (Eq. (5)). While this trait is beneficial at high Reynolds numbers (pressure drop is easily measured and should be minimized to limit head loss), it is the contrary in the case at hand. Therefore, a multi-hole and/or slotted orifice design can be ruled out. This comment

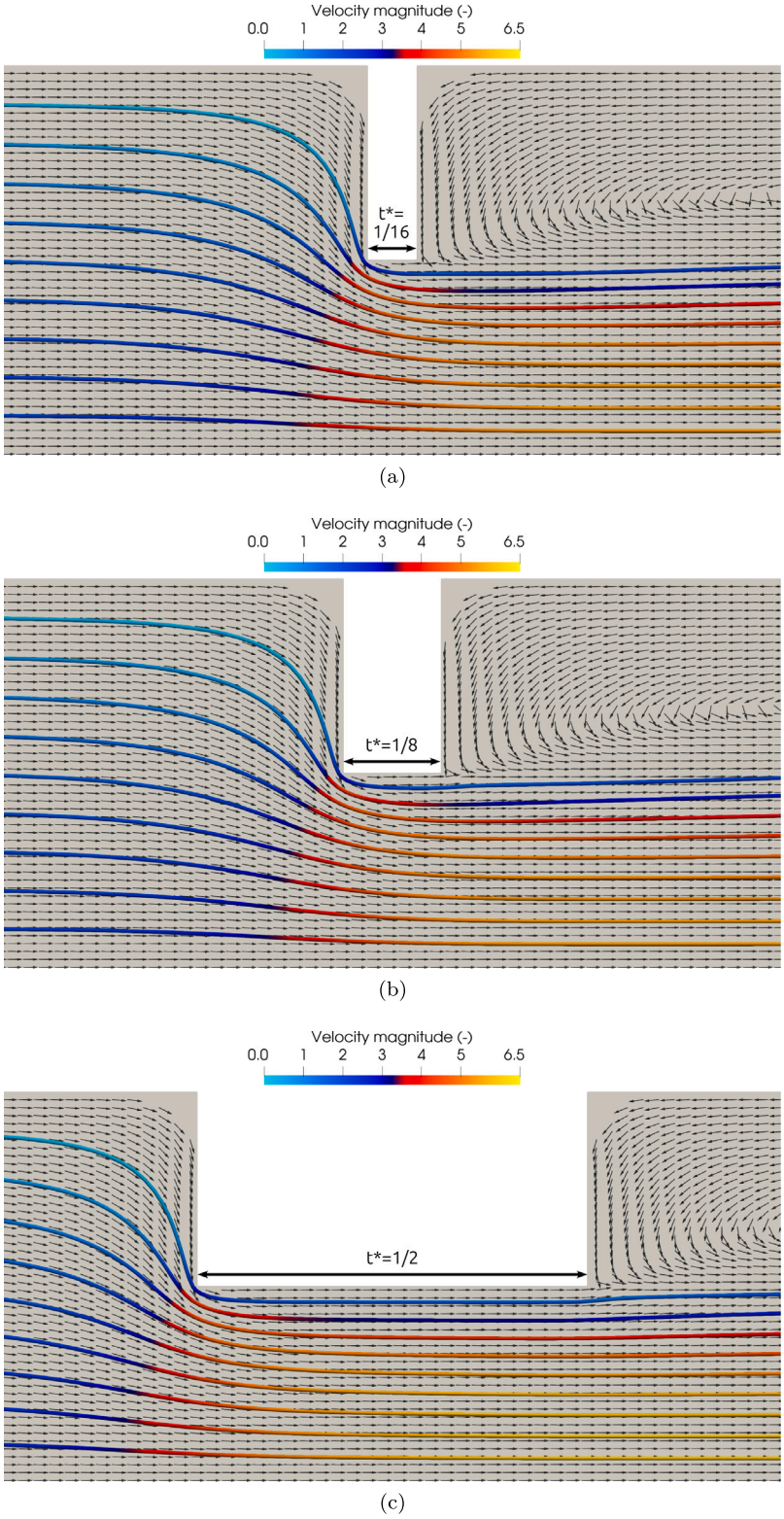

Fig. 8. Close-up view of the flow around the orifice for a β value of 0.5 and a square root of the orifice Reynolds number of 13. Vector field - velocity direction. Tubes - streamlines, colored by velocity magnitude. Top - $t^* = 1/16$. Middle - $t^* = 1/8$. Bottom - $t^* = 1/2$. Domain size −20 to +20 pipe diameters.

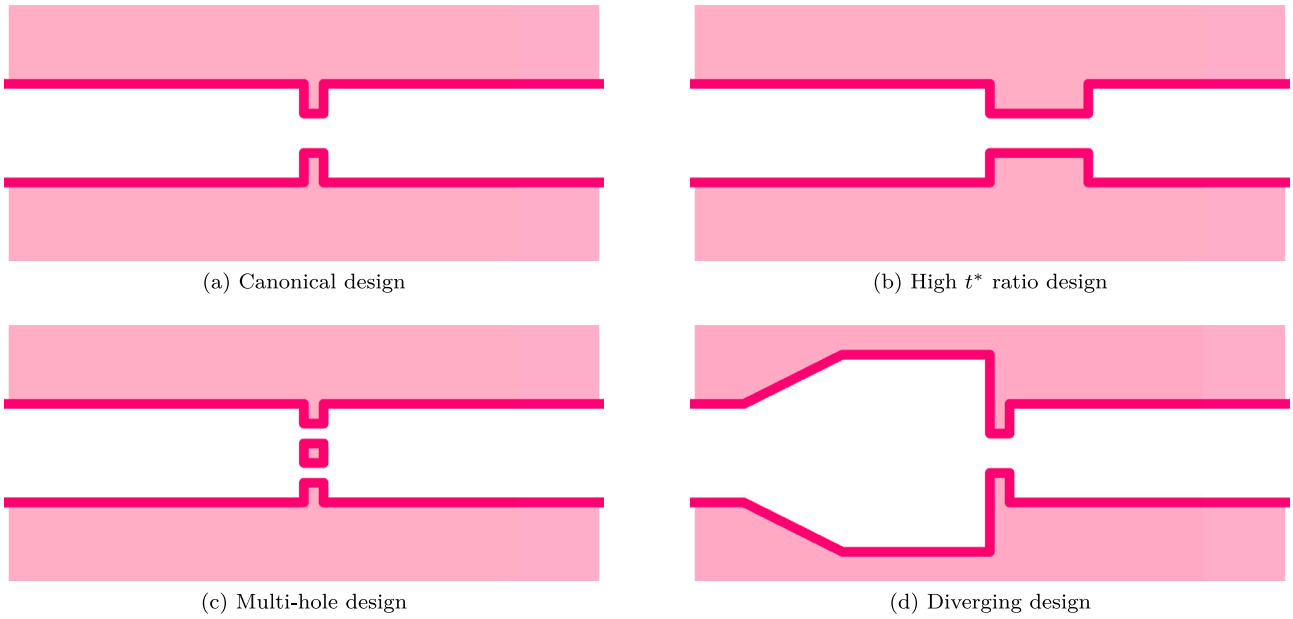

Fig. 9. Four designed envisioned to delineate the design space.

leaves only the manipulation of the β and t^* ratios on the table. Authors agree that in all circumstances the first modulator of the discharge coefficient is the β ratio [17,18]. With this consideration in mind, the diverging design might seem a good idea. Indeed, it would increase the β ratio without resorting to drilling a smaller orifice. Still, working a bit of math out shows that this strategy would offer only marginal modulation. Indeed, when introducing the volumetric flow rate into the equation, one can derive the main dependencies of the pressure with respect to operating parameters (Eq. (6)). Assuming $d < D$, *i.e.*, β is small, which is the case, the pressure drop only depends on the flow rate and the orifice diameter. Therefore, an upstream expansion would not yield any significant performance improvement.

$$\Delta P = \rho U^2 \frac{1-\beta^4}{2\beta^4 C d^2} \tag{5}$$

$$\Delta P = \rho \frac{8Q^2}{\pi^2} \frac{1-\frac{d^4}{D^4}}{d^2 C d^2} \simeq \rho \frac{8Q^2}{\pi^2} \frac{1}{d^4 C d^2} \tag{6}$$

4.2. Tested designs

The above considerations leave only two levers to act on: the orifice thickness and its length. Therefore, a systematic variation of the two parameters was tested over the 1 to 400 pipe Reynolds number range. β ratio was either to 0.05 or 0.10, while the t^* could take the values 0.5 or 1.0. The aim of both low β ratio (defined as below or equal to 0.1, the lower range of the ISO standard [9]) and high t^* ratio is to maximize pressure difference at low flow rate. The simulations were run linearly spread in pipe Reynolds number square root space, to mimic Johansen, Sahin, and Ceyhan's formatting. Still, upon processing the results, they turned out to be more legible in log–log scale (Fig. 10). As one can see, all the designs operating curves follow a clear quadratic downward trend. The β ratio is the first modulator of the Euler number value, while the t^* ratio is a secondary modulator. Furthermore, the latter is only effective at low Reynolds numbers. From a practical point of view, this translates into the fact that increasing the orifice length will increase the pressure at low flow rate, but not substantially modify it under high flow rate conditions. Moving closer to the application, the question of the measurable pressure difference comes into play. As this indicator is dependent on the pipe diameter and the fluid density (Eq. (6)), in the case of air, it depends implicitly on the pressure. Therefore, the limits, given by a minimal and maximal measurable pressure difference of 1 Pa and 10,000 Pa, respectively, were drawn in shaded grey for the extreme pipe diameters classically encountered in biotechnology laboratories (4 and 8 mm).

From a design perspective, none of the tested variations would be able to monitor the flow in the desired range of flow rate and pressure. The one closest to achieving this feat would be the 4 mm diameter pipe setting, with a β ratio of 0.10 and a t^* ratio of 1.0. Also, while not as efficient, it is interesting to note that, in the 8 mm diameter pipe setting, it is the system with a β ratio of 0.05 and a t^* ratio of 1.0 that would yield the best performances. These observations can be difficult to summarize as they mix dimension-bearing and dimensionless features. Taking a step back, and remembering that for low β ratio values, the pressure drop depends primarily upon the orifice diameter (Eq. (6)), it can be concluded that a diameter around 0.4 mm would be a good start. Still, drilling such a small hole seems challenging. Furthermore, imposing the same constraint on both pipe diameters (4 and 8 mm) in terms of minimal flow rate (10 Nml/min) neglects the fact that small-diameter pipes are used for low flow rates, while larger-diameter pipes are used for high flow rates. As this article intends to demonstrate the feasibility of the workflow and not necessarily design a one-size-fits-all solution, nor case-dependent solutions, it will focus on optimizing the system in the 4 mm diameter pipe setting, as it is the most stringent, but unfortunately, the one of direct applicability for the author.

4.3. Conventional machining

Noting the trends and value obtained in the case of a 4 mm diameter pipe (Fig. 10 (Left)), the most economical option would be to lengthen the orifice depth so that the anticipated results would be somewhat above the ones of the yellow curve (β ratio of 0.10 and a t^* ratio of 1.0). This option offers the sizable advantage of bringing the orifice diameter close to 0.5 mm, making it machinable using conventional means. In addition, with the 1/20 hole diameter to support thickness ratio rule of thumb for plastic materials, it allows achieving t^* ratio values as high as 2.0. Therefore, β ratios from 0.08 to 0.12, and t^* ratios from 1.0 to 2.0 were investigated. The adequacy criterion is set to meet the detection criterion, at a flow rate of 10 Nml/min (pipe Reynolds number of 3.46 in a 4 mm diameter pipe), of a pressure drop of at least 1 Pa (minimum Euler number of 1.11 10^5, rounded up to 2.0 10^5). In order to be conservative, the simulations were run at a pipe Reynolds

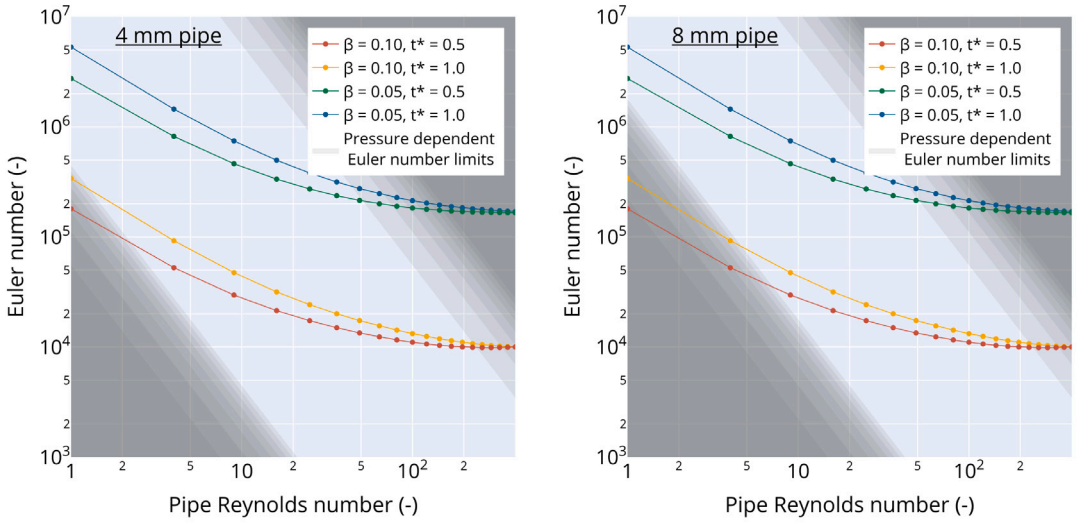

Fig. 10. Euler number versus pipe Reynolds number for the tested designs. Grey shaded area - Minimal and maximal Euler numbers to be achieved based on a minimal measurable pressure difference of 1 Pa and a maximum measurable pressure difference of 10 000 Pa, pressure and pipe diameter dependent.

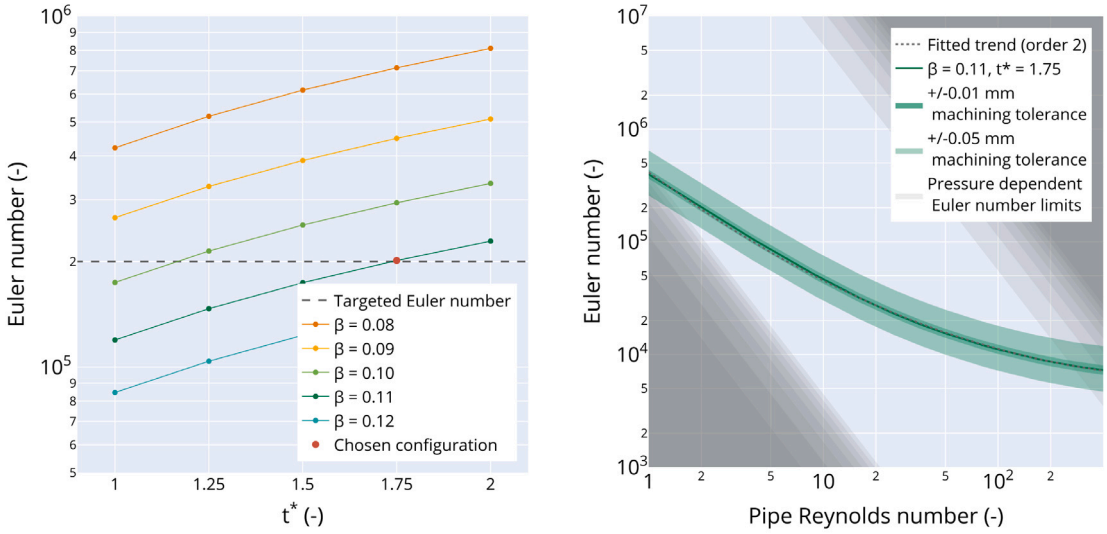

Fig. 11. Left - Euler number at a pipe Reynolds number of 2 for the different geometries (defined by their β and t^* ratios). Right - Euler number versus pipe Reynolds number of the chosen configuration. Green shaded area - impact of machining tolerances. Grey shaded area - Minimal and maximal Euler numbers to be achieved based on a minimal measurable pressure difference of 1 Pa and a maximum measurable pressure difference of 10,000 Pa, pressure and pipe diameter dependent.

number of 2, and the resulting Euler numbers were drawn for all the tested configurations (Fig. 11 (Left)). As one can see, the $\beta = 0.11$ and $t^* = 1.75$ configuration meets the desired criterion and was, therefore, retained.

The retained design was therefore simulated over the targeted range of Reynolds numbers (Fig. 11 (Right)). In addition to the ideal design, four configurations were simulated to account for potential ± 0.01 and 0.05 mm machining tolerances. The results draw several comments. First of all, the retained design fulfills all the desired criteria. It ensures a measurable pressure drop (of at least 1 Pa) over a 10 to 1,000 NmL/min for pressure ranging from 1 to 8 bar, in a 4 mm diameter pipe. Furthermore, the characteristic curve is easy to fit, in log–log scale, using an order 2 polynomial expression. Finally, it offers reasonable accuracy for the tightest machining tolerance (± 0.01 mm), with flow rate estimation error varying from ± 4.6% (best case scenario over the pressure and flow rate ranges) to ± +9.2% (worst case scenario over the pressure and flow rate ranges). The main advantage of this approach is to make the system readily functional, as a newly produced unit could be used relying on the order 2 polynomial expression as a calibration curve (implicitly accepting an uncertainty up to 10%). Still, while achievable, this tolerance can be regarded as tight.

Resorting to a wider margin (± 0.05 mm) induces inadmissible uncertainty (from ± +24.2% to ± +52.1% over the pressure and flow rate ranges). Therefore, for units realized with this level of mechanical tolerance, it would be necessary to calibrate them externally. This can be achieved by setting the unit inline with a mass flow meter and drawing a device-specific calibration curve (recording the pressure drop on the orifice flow meter and the flow rate on the mass flow meter).

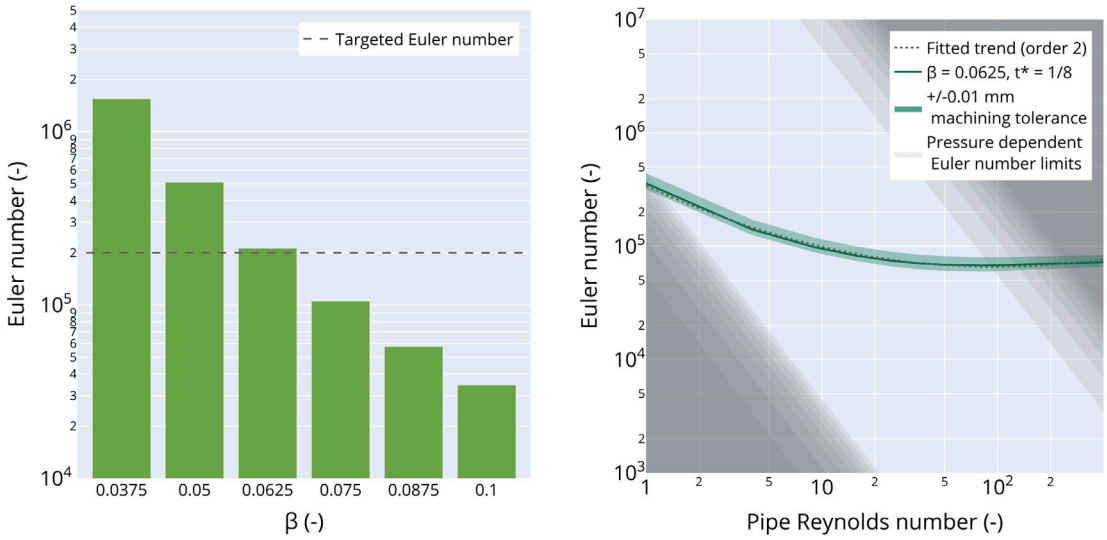

Fig. 12. Left - Euler number at a pipe Reynolds number of 2 for the different geometries (defined by their β, as t^* ratio is fixed at 1/8). Right - Euler number versus pipe Reynolds number of the chosen configuration. Green shaded area - impact of machining tolerances. Grey shaded area - Minimal and maximal Euler numbers to be achieved based on a minimal measurable pressure difference of 1 Pa and a maximum measurable pressure difference of 10,000 Pa, pressure and pipe diameter dependent.

While posing no particular challenge, this procedure is less convenient than having a readily functional system.

4.4. Advanced machining - clockmaking

If one decides to go beyond conventional machining, talented craftsmanship can be brought to the table, such as clockmaking, where experts can drill 0.15 mm diameter holes with a tolerance of ± 0.01 mm. Still, restrictions apply, such as the fact that the metal sheet to be pierced cannot exceed 0.5 mm in thickness. Exploring this avenue would lead to orifice flow meters of variable β ratio (0.0375 to 0.1) but fixed t^* ratio of 1/8 (in the case of a 4 mm diameter pipe). Fig. 12 (Left) reports how such low β ratios would influence the Euler number for a pipe Reynolds number of 2. As one can see, for a β ratio of 0.0625, *i.e.*, an orifice diameter of 0.25 mm, the targeted Euler number can be reached. Analyzing this configuration with a ± 0.01 mm machining tolerance (Fig. 12 (Right)) shows that the system characteristic curve can be fitted satisfactorily with an order 2 polynomial expression. Furthermore, the machining tolerance would result in flow rate estimation error varying from ± 6.5% (best case scenario over the pressure and flow rate ranges) to ± +14.2% (worst case scenario under low flow rate and high pressure conditions). Taking a step back, this approach represents a substantial improvement over the conventional machining high tolerance case (± 0.05 mm). Thus, while an external calibration of the unit remains advisable, it is possible to envision its use out of the box, provided other sources of uncertainty, such as pressure tap realization or temperature/absolute pressure drifts of the pressure sensor, are controlled.

5. Conclusion

The goal of this work was to investigate the feasibility of an affordable low-Reynolds-number flow meter for application in a biotechnology laboratory (10 to 1,000 Nml/min, in 4 to 8 mm diameter pipes, under 1 to 8 bar). For this purpose, the orifice flow meter concept was opted for as it possesses advantages relevant in a biotechnology environment (handling of moist gases, high-pressure operation, robustness against foam/culture backflows, ease of cleaning). CFD was chosen as the means for these investigations. The proposed numerical workflow represents a substantial improvement over existing work. The main advancement is its coverage of the laminar, transition, and turbulent regimes while offering excellent comparison with experiments. Once validated, it was applied to the orifice flow meter design itself. The cornerstones design rules familiar to the community were acknowledged, and a low β ratio, high t^* ratio design emerged. Still, the specific application to biotechnology laboratory flows proved to be a challenge as the required orifice diameter (0.25 or 0.44 mm), while achievable, necessitated a very tight (± 0.01 mm) machining tolerance, or external calibration of each of the units. In a nutshell, while such a flow meter is realizable, it is not a trivial thing.

Nomenclature

Latin symbols	Property	Unit
C_μ	Turbulence model coefficient (0.09)	–
Cd	Discharge coefficient	–
Cs	Smagorinsky coefficient	–
D	Pipe diameter	m
d	Orifice diameter	m
Eu	Euler number	–
f	Vortices frequency	1/s
I	Turbulence intensity	%
k	Turbulent kinetic energy	m^2/s^2
L	Turbulent length	%
l	Turbulent subgrid length	m
n	Surface normal vector	–
p	Pressure	Pa
Q	Volumetric flow rate	m^3/s
R	Pipe radius	m
r	Running radius	m
Re	Reynolds number	–
S	Shear rate tensor	Pa/m
St	Strouhal number	–
U	Reference velocity	m/s
u	Velocity vector	m/s
v	Orifice velocity	m/s
t	Orifice thickness	m
x	Position vector	m
y^+	Dimensionless wall distance	–

Greek & Other symbols	Property	Unit
β	Orifice diameter to pipe diameter ratio	–
γ	Turbulence indicator field	–
Δ	Cell characteristic size (cubic root of the volume)	m
μ	Dynamic viscosity	Pa.s
ν	Kinematic viscosity	m^2/s
ρ	Density	kg/m^3
τ	Time	s
ω	Specific dissipation rate	1/s
∇	Nabla operator	–

Subscript & Superscript	Description
*	Dimensionless
sgs	Sub Grid Scale
θ_t	Momentum deficit Reynolds number triggering the transition
turb	Turbulent

CRediT authorship contribution statement

Victor Pozzobon: Writing – review & editing, Writing – original draft, Visualization, Validation, Software, Methodology, Investigation, Funding acquisition, Formal analysis, Data curation, Conceptualization.

Declaration of competing interest

The authors declare that they have no known competing financial interests or personal relationships that could have appeared to influence the work reported in this paper.

Acknowledgments

The author thanks Pr. Sylvain Salvador, his PhD director for telling him that it was possible to measure a flow rate with an orifice almost fifteen years ago. Communauté urbaine du Grand Reims, Département de la Marne, Région Grand Est and European Union (FEDER Grand Est 2021–2027) are acknowledged for their financial support to the Chair of Biotechnology of CentraleSupélec and the Centre Européen de Biotechnologie et de Bioéconomie (CEBB).

Data availability

No data was used for the research described in the article.

References

[1] S. Weber, S. Schaepe, S. Freyer, M. Kopf, C. Dietzsch, Jet aeration as alternative to overcome mass transfer limitation of stirred bioreactors, Eng. Life Sci. 18 (4) (2018) 244–253, http://dx.doi.org/10.1002/elsc.201700169, URL https://pmc.ncbi.nlm.nih.gov/articles/PMC6999413/.

[2] T. Schweder, E. Krüger, B. Xu, B. Jürgen, G. Blomsten, S.-O. Enfors, M. Hecker, Monitoring of genes that respond to process-related stress in large-scale bioprocesses, Biotechnol. Bioeng. 65 (2) (1999) 151–159, http://dx.doi.org/10.1002/(SICI)1097-0290(19991020)65:2<151::AID-BIT4>3.0.CO;2-V, URL https://onlinelibrary.wiley.com/doi/abs/10.1002/%28SICI%291097-0290%2819991020%2965%3A2%3C151%3A%3AAID-BIT4%3E3.0.CO%3B2-V, _eprint: https://analyticalsciencejournals.onlinelibrary.wiley.com/doi/pdf/10.1002/%28SICI%291097-0290%2819991020%2965%3A2%3C151%3A%3AAID-BIT4%3E3.0.CO%3B2-V.

[3] S. Gao, S. Edmundson, M. Huesemann, Oxygen stress mitigation for microalgal biomass productivity improvement in outdoor raceway ponds, Algal Res. 68 (2022) 102901, http://dx.doi.org/10.1016/j.algal.2022.102901, URL https://www.sciencedirect.com/science/article/pii/S2211926422002727.

[4] J. Hanotu, D. Kong, W.B. Zimmerman, Intensification of yeast production with microbubbles, Food Bioprod. Process. 100 (2016) 424–431, http://dx.doi.org/10.1016/j.fbp.2016.07.013, URL https://www.sciencedirect.com/science/article/pii/S0960308516300852.

[5] F.M. White, Fluid Mechanics, Mcgraw-Hill College, Boston, 1999.

[6] F.C. Johansen, Flow through pipe orifices at low Reynolds numbers, Proc. R. Soc. Lond. Ser. A, Contain. Pap. A Math. Phys. Character 126 (801) (1930) 231–245, URL https://www.jstor.org/stable/95350.

[7] R.T. Page, Constant-flow orifice meters of low capacity, Ind. Eng. Chem. Anal. Ed. 7 (5) (1935) 355–358, ISBN: 0096-4484.

[8] H.E. Merritt, Hydraulic Control Systems, Wiley, New York, 1967.

[9] Measurement of fluid flow by means of pressure differential devices inserted in circular cross-section conduits running fullPart 2: Orifice plates, 2003, URL https://www.iso.org/standard/30190.html.

[10] A. Golijanek-Jedrzejczyk, A. Mrowiec, Cylindrical orifice testing in laminar flow with the orifice diameter ratio Beta=0.5, Sci. Rep. 13 (1) (2023) 15411, http://dx.doi.org/10.1038/s41598-023-42451-0, URL https://www.nature.com/articles/s41598-023-42451-0.

[11] W. Borutzky, B. Barnard, J. Thoma, An orifice flow model for laminar and turbulent conditions, Simul. Model. Pr. Theory 10 (3) (2002) 141–152, http://dx.doi.org/10.1016/S1569-190X(02)00092-8, URL https://www.sciencedirect.com/science/article/pii/S1569190X02000928.

[12] M.S. Shah, J.B. Joshi, A.S. Kalsi, C.S.R. Prasad, D.S. Shukla, Analysis of flow through an orifice meter: CFD simulation, Chem. Eng. Sci. 71 (2012) 300–309, http://dx.doi.org/10.1016/j.ces.2011.11.022, URL https://www.sciencedirect.com/science/article/pii/S0009250911008219.

[13] E. Muñoz-Díaz, F.J. Solorio-Ordaz, G. Ascanio, A numerical study of an orifice flowmeter, Flow Meas. Instrum. 26 (2012) 85–92, http://dx.doi.org/10.1016/j.flowmeasinst.2012.03.012, URL https://www.sciencedirect.com/science/article/pii/S0955598612000295.

[14] B. Sahin, H. Ceyhan, Numerical and experimental analysis of laminar flow through square-edged orifice with variable thickness, Trans. Inst. Meas. Control 18 (4) (1996) 166–174, http://dx.doi.org/10.1177/014233129601800401.

[15] T. Tunay, B. Sahin, H. Akilli, Investigation of laminar and turbulent flow through an orifice plate inserted in a pipe, Trans. Can. Soc. Mech. Eng. 28 (2B) (2004) 403–414, http://dx.doi.org/10.1139/tcsme-2004-0029, URL https://cdnsciencepub.com/doi/abs/10.1139/tcsme-2004-0029.

[16] V.K. Singh, T. John Tharakan, Numerical simulations for multi-hole orifice flow meter, Flow Meas. Instrum. 45 (2015) 375–383, http://dx.doi.org/10.1016/j.flowmeasinst.2015.08.004, URL https://www.sciencedirect.com/science/article/pii/S0955598615300054.

[17] M. Đurđević, M. Bukurov, S. Tasin, S. Bikić, Experimental research of single-hole and multi-hole orifice gas flow meters, Flow Meas. Instrum. 70 (2019) 101650, http://dx.doi.org/10.1016/j.flowmeasinst.2019.101650, URL https://www.sciencedirect.com/science/article/pii/S0955598619301967.

[18] A. Tomaszewski, T. Przybylinski, M. Lackowski, A. Tomaszewski, T. Przybylinski, M. Lackowski, Experimental and numerical analysis of multi-hole orifice flow meter: Investigation of the relationship between pressure drop and mass flow rate, Sensors 20 (24) (2020) http://dx.doi.org/10.3390/s20247281, URL https://www.mdpi.com/1424-8220/20/24/7281, Company: Multidisciplinary Digital Publishing Institute Distributor: Multidisciplinary Digital Publishing Institute Institution: Multidisciplinary Digital Publishing Institute Label: Multidisciplinary Digital Publishing Institute.

[19] G.L. Morrison, D. Terracina, C. Brewer, K.R. Hall, Response of a slotted orifice flow meter to an air/water mixture, Flow Meas. Instrum. 12 (3) (2001) 175–180, http://dx.doi.org/10.1016/S0955-5986(01)00018-8, URL https://www.sciencedirect.com/science/article/pii/S0955598601000188.

[20] J.A. Fedchak, D.R. Defibaugh, Accurate conductance measurements of a pinhole orifice using a constant-pressure flowmeter, Measurement 45 (10) (2012) 2449–2451, http://dx.doi.org/10.1016/j.measurement.2011.10.046, URL https://www.sciencedirect.com/science/article/pii/S0263224111004088.

[21] H. Yoshida, M. Hirata, T. Hara, Y. Higuchi, Comparison of measured leak rates and calculation values for sealing packages, Packag. Technol. Sci. 34 (9) (2021) 557–566, http://dx.doi.org/10.1002/pts.2594, URL https://onlinelibrary.wiley.com/doi/abs/10.1002/pts.2594, _eprint: https://onlinelibrary.wiley.com/doi/pdf/10.1002/pts.2594.

[22] R.B. Langtry, F.R. Menter, Correlation-based transition modeling for unstructured parallelized computational fluid dynamics codes, AIAA J. 47 (12) (2009) 2894–2906, http://dx.doi.org/10.2514/1.42362, URL https://arc.aiaa.org/doi/10.2514/1.42362.

[23] F.R. Menter, Improved two-equation k-omega turbulence models for aerodynamic flows, Tech. Rep. A-92183, 1992, URL https://ntrs.nasa.gov/citations/19930013620, NTRS Author Affiliations: NASA Ames Research Center NTRS Document ID: 19930013620 NTRS Research Center: Legacy CDMS (CDMS).

[24] S. Vemulapalli, S.K. Venkata, Parametric analysis of orifice plates on measurement of flow: A review, Ain Shams Eng. J. 13 (3) (2022) 101639, http://dx.doi.org/10.1016/j.asej.2021.11.008, URL https://www.sciencedirect.com/science/article/pii/S2090447921004172.

[25] V. Yakhot, S.A. Orszag, S. Thangam, T.B. Gatski, C.G. Speziale, Development of turbulence models for shear flows by a double expansion technique, Phys. Fluids A: Fluid Dyn. 4 (7) (1992) 1510–1520, http://dx.doi.org/10.1063/1.858424, URL https://doi.org/10.1063/1.858424.

[26] P. Testud, Y. Aurégan, P. Moussou, A. Hirschberg, The whistling potentiality of an orifice in a confined flow using an energetic criterion, J. Sound Vib. 325 (4) (2009) 769–780, http://dx.doi.org/10.1016/j.jsv.2009.03.046, URL https://www.sciencedirect.com/science/article/pii/S0022460X09002995.

[27] B. Merci, E. Dick, J. Vierendeels, C. De Langhe, Determination of Epsilon at inlet boundaries, Internat. J. Numer. Methods Heat Fluid Flow 12 (1) (2002) 65–80, http://dx.doi.org/10.1108/09615530210413172.

[28] N.T. Basse, Turbulence intensity and the friction factor for smooth- and rough-wall pipe flow, Fluids 2 (2) (2017) http://dx.doi.org/10.3390/fluids2020030, URL https://www.mdpi.com/2311-5521/2/2/30, Company: Multidisciplinary Digital Publishing Institute Distributor: Multidisciplinary Digital Publishing Institute Institution: Multidisciplinary Digital Publishing Institute Label: Multidisciplinary Digital Publishing Institute.

[29] J.G. Baker, J.R. van Meter, Reducing reflections from mesh refinement interfaces in numerical relativity, Phys. Rev. D 72 (10) (2005) 104010, http://dx.doi.org/10.1103/PhysRevD.72.104010, URL https://link.aps.org/doi/10.1103/PhysRevD.72.104010.

[30] S.J. Rees, M.P. Juniper, The effect of confinement on the stability of viscous planar jets and wakes, J. Fluid Mech. 656 (2010) 309–336, http://dx.doi.org/10.1017/S0022112010001060, URL https://www.cambridge.org/core/journals/journal-of-fluid-mechanics/article/abs/effect-of-confinement-on-the-stability-of-viscous-planar-jets-and-wakes/638122F401339FAE1B93DCBA19A9E019.

[31] J.C. Hunt, A.A. Wray, P. Moin, Eddies, streams, and convergence zones in turbulent flows, in: Studying Turbulence using Numerical Simulation Databases, 2. Proceedings of the 1988 Summer Program, 1988, URL https://ntrs.nasa.gov/citations/19890015184.

[32] J.E. Nash, J.V. Sutcliffe, River flow forecasting through conceptual models part I A discussion of principles, J. Hydrol. 10 (3) (1970) 282–290, http://dx.doi.org/10.1016/0022-1694(70)90255-6, URL https://www.sciencedirect.com/science/article/pii/0022169470902556.

[33] L.I.-K. Lin, A concordance correlation coefficient to evaluate reproducibility, Biometrics 45 (1) (1989) 255–268, http://dx.doi.org/10.2307/2532051, URL https://www.jstor.org/stable/2532051.

[34] I.B. Celik, U. Ghia, P.J. Roache, C.J. Freitas, Procedure for estimation and reporting of uncertainty due to discretization in CFD applications, J. Fluids Engineering-Transactions ASME 130 (7) (2008) ISBN: 0098-2202.

[35] K. Kadoya, N. Matsunaga, A. Nagashima, Viscosity and thermal conductivity of dry air in the gaseous phase, J. Phys. Chem. Ref. Data 14 (4) (1985) 947–970, http://dx.doi.org/10.1063/1.555744.